Mechatronics of Electrostatic Microactuators for Computer Disk Drive Dual-Stage Servo Systems

Yunfeng Li and Roberto Horowitz

Abstract— **A decoupled track-following control architecture and discrete time pole placement design methodology are proposed for dual-stage servo systems in magnetic hard disk drives. The methodology was applied to the design of a control system for a dual-stage servo with a MEMS microactuator (MA) that rotates the slider relative to the gimbal. MIMO and SIMO controllers were design for the cases when the relative position error signal (RPES) of the MA relative to the suspension is respectively available and not available to the control system. The effect of MA resonance variations on the stability and performance of the controller were analyzed for both cases. A self-tuning scheme was developed to tune the control parameters, in order to compensate for variations in the microactuators' resonance mode.**

Keywords— **Hard disk drive, servo control, dual stage.**

I. Introduction

IT is predicted future areal storage density increases in magnetic disk drive will be achieved mainly through an increase in track density. For a predicted bit aspect ratio of 4:1, an areal density of 100 Gb/in^2 translates to a linear bit density of 672k bits per inch (BPI), and a radial track density of 168k tracks per inch (TPI), which in turn implies a track pitch of 150 nm. In order to achieve an ultimate 10-fold increase in TPI, it will be necessary to develop high bandwidth, robust track-following servo systems. Dual-stage actuation has been proposed as a means of increasing the necessary servo bandwidth to achieve the required runout and disturbances rejections.

Two dual-stage actuation approaches for magnetic disk drives are currently being considered by the magnetic recording industry. In the first approach, which is generally referred to as the actuated suspension, mini-actuators (usually made of piezoelectric materials such as PZT) are used to flex the suspension around a pivot, producing relative motion of the read/write head along the radial direction. However, most actuated suspensions have multiple structural resonance modes in the 4 -12 kHz frequency range, which may limit the bandwidth of the servo system. The second approach to dual-stage actuation utilizes Micro-electromechanical Systems (MEMS), and is generally referred to as the actuated slider approach [1], [2]. In this approach, an electrostatic or electromagnetic MEMS fabricated microactuator (MA) is sandwiched between the gimbal and the slider and it either rotates or translates the slider relative to the suspension. The actuated slider approach achieves a truly collocated second stage actuation of the read/write head, bypassing nonlinear friction, bias forces, and all E-block, suspension and gimbal structural resonance modes. Usually, MEMS MA has a single flexure resonance mode in the 1-2 kHz frequency range, and has no other appreciable structural resonance mode up the 40 kHz frequency range [1]. Thus, the MEMS MA actuated slider dual-stage approach may provide a potential high performance and low cost solution to achieving extremely high track density, since the MEMS MA can be batch fabricated, and micro-assembled with the head and the gimbal of suspension.

The resonance frequency of MEMS MA's lightly damped flexure resonance mode is relatively low and close to the open loop gain crossover frequency of the servo system. Furthermore, due to lithographic misalignment and variations present in the etching processes, the actual resonance frequency of the MA can vary by as much as $\pm$ 15% from its designed nominal value. Thus, the controller robustness to the uncertainty in the MA's resonance frequency must be considered for MEMS based dual-stage servo control design. Another difference between PZT actuated suspension and MEMS based dual-stage system is the availability of a sensor that can measure the displacement of the read/write head, relative to the suspension. In most PZT actuated suspensions, relative position sensing is generally not available and the dual-stage controller must be single-input-multi-output (SIMO). While for most MEMS MA, capacitive sensing can be used to measure the MA's relative position [2], and the dual-stage controller can potentially be multi-input-multi-output (MIMO).

Several controller design methods have been proposed for PZT actuated suspension dual-stage systems [4], [5], [6], [7]. Controller designs for MEMS based dual-stage servo systems have been reported in [8] and [9]. In [8], a SIMO controller was designed using a parallel design technique. However, the robustness of the servo system to variations in the microactuator resonance mode was not addressed. In [9], robust SIMO and MIMO H_∞ optimal controllers were designed using μ-synthesis. In this paper, we present a decoupled discrete time pole placement design method which can be used for both SIMO and MIMO controllers designs. The decoupling design approach utilized in this paper was originally introduced in [10], for use in a PZT actuated suspension. Compared with the μ-synthesis design in [9], the implementation of the controller designed using this method requires significantly less computations. Moreover, the dual-stage decoupled control architecture is amenable to the incorporation of a self-tuning algorithm for compensating variations in the MA's resonance frequency.

The paper is organized as follows. A MEMS based dual-

Research supported by the National Storage Industry Consortium (NSIC) and the Computer Mechanics Laboratory (CML) of U.C. Berkeley.

Y. Li and R. Horowitz are with the Department of Mechanical Engineering of the University of California at Berkeley, CA 94720-1740, USA. Corresponding author's e-mail: horowitz@me.berkeley.edu.

stage actuator model is briefly discussed in Section II. In Section III, the decoupled controller design structure and discrete time sensitivity transfer function design process are presented. The robustness of the designs is analyzed in Section IV using μ analysis. In Section V, a self-tuning control algorithm for the MA minor loop is formulated. Conclusions were provided in Section VI.

II. Dual-stage model with a MEMS MA

L.-S. Fan and his co-workers at the IBM Almaden Research Center (ARC) have developed an innovative etching and electroplating multi-layer technology for fabricating high-aspect-ratio MEMS devices [1]. This fabrication process can be implemented at IBM's existing head manufacturing facilities, which annually produce hundreds of millions of thin-film heads. The process includes high aspect ratio Transformer-Coupled Plasma (TCP) reactive-ion etching (RIE), which achieves a 20:1 height to width aspect ratio on 40 mm thick polymers. The etched polymers are in turn used as molds to fabricate, through a metal electroplating process, high-aspect ratio invar (a nickel-iron-based alloy) micro-structures. Area efficient electrostatic rotational MAs have been successfully designed and fabricated using this process. Fig. 1 shows a photograph of such a device mounted on an integrated lead suspension. A pico-slider is attached on top of the MA. Electrical

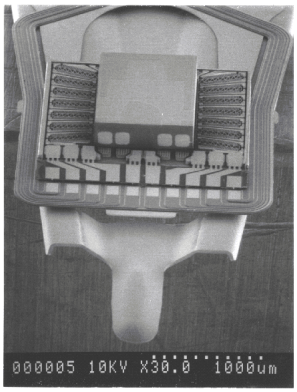

Fig. 1. 1 IBM's electrostatic MA mounted on an integrated lead suspension. (Courtesy of L.-S. Fan.)

contacts between the slider and MA are made using laser reflow. The electrostatic MA is assembled on to the gimbal of an integrated lead suspension, and rotates the pico-slider about its center of mass, using an area-efficient layout of electrostatically actuated comb-fingers.

Since the pico-slider flies on top of the disk on an air bearing, the MA must support a gram of out-of-plane loading, with minimum out-of-plane deflection. Thus, the MA's flexures must be very stiff in the out-of-plane direction, while compliant in the in-plane radial direction to have enough DC gain. A 400:1 out-of-plane to in-plane stiffness ration was achieved by the 20:1 height to width flexure aspect ratio in the fabrication process described above. Because of out-of-plane deflection constraints, the combined MA pico slider assembly was designed to have a nominal in-plane rotational flexural resonance frequency of 1.5 kHz. Variations in the etching process and lithographic misalignments cause $\pm$ 15% variations in the MA's resonance frequency from its designed nominal value. Beside this single lightly damped resonance mode, the MA does not have other appreciable structural dynamics up to 40 kHz frequency range. Thus, its dynamics can be adequately described by a simple mass-spring-damper second order transfer function [1], [3]

$$G_M(s) = \frac{A_M}{s^2 + 2\zeta_{MO}\omega_{MO}\, s + {\omega_{MO}}^2}\,. \tag{1}$$

Table I provides values for the parameters in Eq. (1) as well as other important parameters of the IBM MA model, on which the designs in this paper are based.

Res. Freq. ω_{MO}	Damping Coeff. ζ_{MO}	Stroke limit	Acc. Gain A_M	Max. Voltage
1.5 kHz $\pm$15%	0.015	$\pm$1 μm	2 G/V	$\pm$40 V

TABLE I
IBM's Electrostatic MA Parameters

A rotational MA design was selected, in order to counteract the hundreds' G in plane acceleration that is exerted to the pico-slider's center of mass by the VCM during a seek operation. Given the fact that the torque produced by the electrostatic MA is in the one tenth of μN-mm range, its reaction on the suspension can be neglected. In addition, the pico-slider is mounted on the MA in a way that its center of mass coincides with the actuator's axis of in plane rotation. Thus, the acceleration induced by the VCM on the pico-slider's center of mass has little effect on the MA's response. As a consequence, the open loop dynamics between the VCM and MA control inputs and the corresponding head motion can be described by an uncoupled block diagram shown in Fig. 2, where i_V is the electrical current input to the VCM, v_M is the voltage input to the MA. G_V and G_M are respectively the VCM and MA transfer functions (TF). x_P is the position of the read/write head. It is the summation of the position of the VCM actuator, x_v (more precisely, the position of the tip of the suspension), and the position of the MA relative to the suspension, $RPES$.

$$x_p = x_v + RPES \tag{2}$$

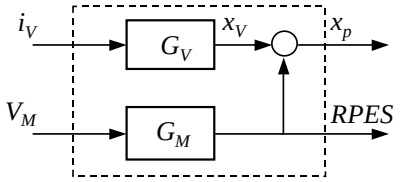

Fig. 2. Dual-Stage Block Diagram

Capacitive sensing can be used in MEMS electrostatic MAs, to measure the $RPES$ [2]. However, this requires

additional sensing electronics and wires to and from the head gimbal assembly (HGA), which may result in an unacceptable increase in the MA's fabrication and assembly costs. Thus, whether or not the $RPES$ will be used in MEMS dual-stage servo systems is still an open question. In this paper, we will classify dual-stage track-following controllers into two categories, according to the availability of the $RPES$: those utilizing the $RPES$ will be called multi-input-multi-output (MIMO) controllers, while those not utilizing the $RPES$ will be called single-input-multi-output (SIMO) controllers.

III. Decoupled track following controller design

The block diagram for a MIMO decoupling control design proposed in this paper is shown in Fig. 3. The part

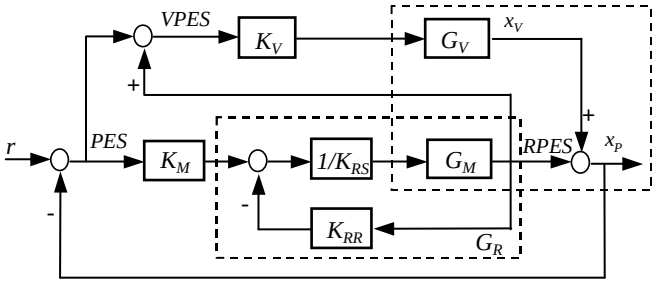

Fig. 3. Dual-stage control design block diagram

enclosed in the dashed box on the upper-right corner of Fig. 3 is the open loop system described in Fig. 2. r represents the track runout, PES is position error signal of the head relative to the data track center (i.e. $PES = r - x_P$), while $RPES$ is the position error signal of the head relative to the tip of the suspension (i.e. $RPES = x_P - x_v$).

The decoupling control approach, originally introduced by [10], utilizes the PES and $RPES$ to generate the position error of the suspension tip relative to the data track center, which will be labeled $VPES$,

$$VPES = PES + RPES = r - x_v, \tag{3}$$

and this signal is feed directly to the VCM compensator. [1]

In the block diagram shown in Fig. 3, there are three compensators that need to be designed: the VCM loop compensator K_V; the MA PES loop compensator K_M; and the MA $RPES$ minor loop compensator K_{RR}/K_{RS}. K_{RR}/K_{RS} is used to damp the MA's flexure resonance mode and place the closed loop poles of the MA $RPES$ loop at an appropriate location. The damped MA closed loop transfer function G_R, shown in the lower-middle dashed box, is defined as

$$G_R = \frac{G_M}{K_{RS} + G_M\, K_{RR}}\,, \tag{4}$$

[1] In [10] the $RPES$ signal was not assumed to be available and was estimated with an open loop observer gain.

while the total dual-stage open loop TF from r to x_P, G_T, is given by

$$G_T = K_V\, G_V + K_M\, G_R + K_M\, G_R\, K_V\, G_V\,. \tag{5}$$

The block diagram in Fig. 3 is equivalent to the sensitivity block diagram shown in Fig. 4, and the total closed

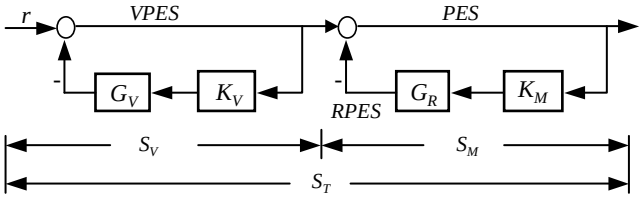

Fig. 4. The sensitivity block diagram

loop sensitivity TF from r to PES is the product of the VCM and MA loop sensitivities, respectively S_V and S_M:

$$S_T = \frac{1}{1+G_T} = S_V\, S_M\,, \tag{6}$$

where

$$S_V = \frac{1}{1+K_V\, G_V}\,, S_M = \frac{1}{1+K_M\, G_R}\,. \tag{7}$$

Thus, the dual stage servo control design can be decoupled into two independent designs: the VCM loop, whose error rejection loop sensitivity TF is given by S_V in Eq. (7), and the MA loop, whose error rejection loop sensitivity TF is given by S_M in Eq. (7).

A. VCM closed loop sensitivity S_V

The VCM loop compensator K_V is designed to attain a desired VCM closed loop sensitivity S_V. Its bandwidth is generally limited by the E-block and suspension resonance modes. The design of this compensator can be accomplished using conventional SISO frequency shaping techniques and will not be discussed here in detail. For illustration purposes, a $6th$ order model of the VCM, which includes torsional and sway resonance modes of the suspension at 2.4 kHz and 5 kHz respectively, was utilized in our simulation study and a $4th$ order compensator K_V running at a 20 kHZ sampling rate was designed to have an approximated bandwidth of $\omega_{_{VC}} = 500Hz$. The gain Bode plot of the resulting sensitivity TF S_V is shown in Fig. 5.

B. MA closed loop sensitivity S_M

The MA loop controller is designed to increase the overall close loop sensitivity attenuation. This design process is explained in detailed in section III-C, after we review the pole-placement design methodology applied to the MEMS MA.

B.1 MA RPES minor loop controller design by pole placement

The zero-order-hold discrete time transfer function for the MA model given in Eq. (1) is

$$G_M(q^{-1}) = \frac{q^{-1}\, B_o(q^{-1})}{A_o(q^{-1})}\,, \tag{8}$$

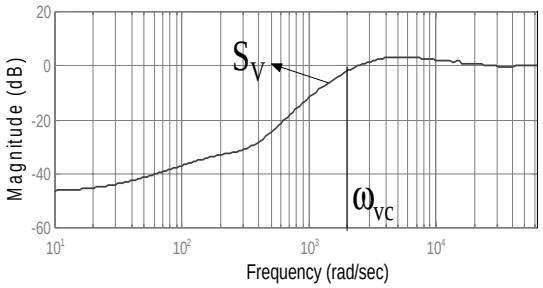

Fig. 5. VCM Loop Sensitivity S_V Magnitude Bode Plot

where q^{-1} is one step delay operator and $B_o(q^{-1})$ and $A_o(q^{-1})$ are respectively the MA open loop zero and pole polynomials:

$$B_o(q^{-1}) = b_o(1 + z_o q^{-1}) \quad (9)$$

$$A_o(q^{-1}) = 1 + a_1\, q^{-1} + a_2\, q^{-2} \quad (10)$$

$$\sigma_o = \zeta_{MO}\,\omega_{MO}\,,\ \omega_{do} = \omega_{MO}\sqrt{1-{\zeta_{MO}}^2}\,,\ p_o = e^{-\sigma_o T}\,, \quad (11)$$

$$a_1 = -2\,p_o\cos(\omega_{do}T)\,,\ a_2 = {p_o}^2\,, \quad (12)$$

$$z_o = \frac{p_o(p_o + \frac{\sigma_o}{\omega_{do}}\sin(\omega_{do}T) - \cos(\omega_{do}T))}{1 - p_o(\cos(\omega_{do}T) + \frac{\sigma_o}{\omega_{do}}\sin(\omega_{do}T)}\,, \quad (13)$$

where T is the controller sampling time and ω_{MO} and ζ_{MO} are respectively the MA's natural frequency and damping ratio, given by table I.

Consider now the RPES minor loop feedback system enclosed by the dashed box in the lower part of Fig. 3 and the resulting MA closed loop TF $G_R(q^{-1})$ defined by Eq. (4). Its poles can be placed by solving the following Diophantine equation [11]

$$A_R(q^{-1}) = A_o(q^{-1})K_{RS}(q^{-1}) + q^{-1}B_o(q^{-1})K_{RR}(q^{-1})\,. \quad (14)$$

The closed loop polynomial $A_R(q^{-1})$ in (14) is chosen by the designer and its roots are the damped MA poles. It is convenient to define the second order polynomial $A_R(q^{-1})$ in an analogous manner to the open loop polynomial $A_o(q^{-1})$ in Eq. (10), in terms of the equivalent continuous time natural frequency ω_{MR} and damping ratio ζ_{MR}, (i.e. substitute ω_{MO} and ζ_{MO} respectively by ω_{MR} and ζ_{MR} in Eq.(11)). ω_{MR} is a design parameter which will be specified later on and normally $\zeta_{MR} \geq 1$. When $A_R(q^{-1})$ is second order the RPES minor loop polynomials $K_{RS}(q^{-1})$ and $K_{RR}(q^{-1})$ are both first order. The resulting closed loop transfer function G_R is given by

$$G_R = \frac{q^{-1}\,B_o(q^{-1})}{A_R(q^{-1})}\,. \quad (15)$$

B.2 MA outer loop controller design by pole placement

Consider now the design of the MA outer loop compensator $K_M(q^{-1}) = K_{MR}(q^{-1})/K_{MS}(q^{-1})$ and assume that the RPES closed loop transfer function G_R is given by (15). The resulting MA closed loop sensitivity transfer function S_M, which was defined in Eq. (7), is given by

$$S_M(q^{-1}) = \frac{A_R(q^{-1})\,K_{MS}(q^{-1})}{A_M(q^{-1})}\,, \quad (16)$$

where the MA outer loop closed loop polynomial $A_M(q^{-1})$ must be chosen by the designer. MA outer loop compensator $K_M(q^{-1}) = K_{MR}(q^{-1})/K_{MS}(q^{-1})$ is generated by solving the following Diophantine equation

$$A_M(q^{-1}) = A_R(q^{-1})K_{MS}(q^{-1}) + q^{-1}B_o(q^{-1})K_{MR}(q^{-1})\,, \quad (17)$$

As in section III-B.1, it is convenient to define the second order polynomial $A_M(q^{-1})$ in terms of the equivalent continuous time natural frequency ω_{MC} and damping ratio ζ_{MC}, where $\omega_{MC} > \omega_{MR}$ and normally $\zeta_{MC} \geq 1$ (i.e. define $A_M(q^{-1})$ as $A_o(q^{-1})$ in Eq. (11), substituting ω_{MO} and ζ_{MO} respectively by ω_{MC} and ζ_{MC}).

The gain Bode plot of the sensitivity TF S_M is shown in Fig. 6, for the case when $\omega_{MC} = 2.4kHz$, $\omega_{MR} = 300Hz$, $\zeta_{MR} = \zeta_{MC} = 1$ and a 20 kHZ sampling rate. For $\zeta_{MR} = \zeta_{MC} = 1$, the low frequency attenuation of S_M is given by

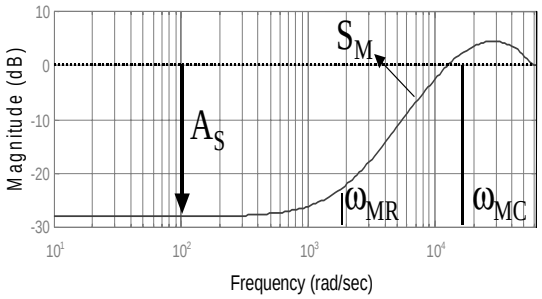

Fig. 6. MA Loop Sensitivity S_M Magnitude Bode Plot

$$A_S = \left(\frac{1-p_{MR}}{1-p_{MC}}\right)^2\left[1 + z_o - z_o\left(\frac{z_o + p_{MC}}{z_o + p_{MR}}\right)^2\right]\,, \quad (18)$$

where z_o is the open loop MA zero given by Eq. (13), $p_{MR} = e^{-\omega_{MR}T}$, $p_{MC} = e^{-\omega_{MC}T}$ and T is the sampling time. Notice that $\lim_{T\to 0} A_S = (\omega_{MR}/\omega_{MC})^2$. Thus, the ratio $(\omega_{MR}/\omega_{MC})^2$ can be used to roughly determine the increased attenuation provided by the MA.

The design procedure has to be modified slightly to account for controller computational time delay. Computational time delay introduces an additional stable zero in the MA transfer function Eq. (8), which can be canceled by the $RPES$ minor controller, and moves the zero z_o in Eq. (18) outside of the unit circle.

C. Dual-stage close loop sensitivity S_T

The MIMO dual-stage servo system depicted in Fig 3 can be designed by a three step design process, which is based on Eqs. (6) - (18) and the sensitivity Bode plots in Figs 5 and 6, and is schematically illustrated by Fig.7.

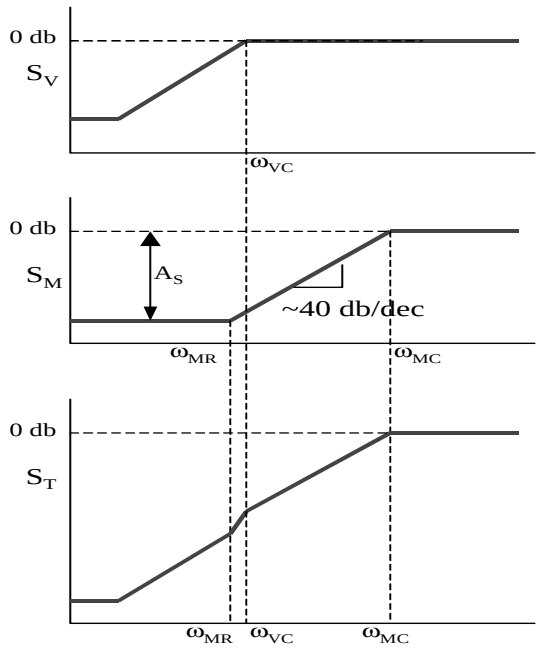

Fig. 7. Illustration of dual-stage sensitivity S_T design

First, the VCM compensator K_V is designed to attain a desired VCM closed loop sensitivity S_V. In a typical design, the VCM bandwidth, ω_{VC} in Fig. 7 is limited by the existence of E-block and suspension resonance modes to be between 400-700 Hz. Subsequently, the MA compensators are designed to attain the additional attenuation, A_s, provided by the MA closed loop sensitivity S_M. As discussed in section III-B, this is accomplished by a two step process. First, the minor $RPES$ loop compensators, K_{RR}/K_{RS}, are designed in order to damp the MA resonance mode and place the poles of G_R, at a desired location. This involves the solution of the Diophantine equation (17). Since the poles of G_R become zeros of S_M, this is equivalent to placing the first corner frequency ω_{MR} of S_M in Fig. 7. Finally, the PES loop compensator K_M is designed to determine the overall bandwidth ω_{MC} of the MA loop closed loop sensitivity S_M. This can also be achieved by pole placement, or other loop shaping techniques.

ω_{MC} is limited by the PES sampling frequency, which is assumed to be 20 kHz in this paper, and the controller computational time delay, which was estimated to be 1/3 the controller sampling time. [12] developed guidelines for determining the allowable servo bandwidth based on the available sampling time and the computational delay time and suggest a bandwidth ω_{MC} of approximately 2.5 kHz for the above mentioned sample rate and computational delay time.

The total dual-stage sensitivity S_T, is schematically shown in the bottom part of Fig. 7. For a given PES sampling rate T bandwidth ω_{MC}, the additional attenuation A_S provided by the MA loop will be determined by the selection of the RPES lower corner frequency ω_{MR}. Since selecting ω_{MR} to be larger than the VCM loop bandwidth ω_{VC}, results in an unnecessary decrease in attenuation A_S. We proposed that ω_{MR} be initially chosen to be the same as ω_{VC}. It can subsequently be adjusted so that the desired attenuation and phase margin requirements of the overall dual stage system are met. Decreasing ω_{MR} increases the low frequency attenuation of S_T. However, this generally reduces the phase margin of the overall open loop transfer function G_T in Eq. (5).

Notice from Eq. (5) that, when ω_{MC} is significantly larger than ω_{VC}, the high frequency response of G_T is dominated by the MA open loop transfer function $K_M\,G_R$ and the gain crossover frequency and phase margin of G_T are slightly smaller than those of the MA open loop given by $K_M\,G_R$, as evidenced by Fig. 8. Notice that decreasing ω_{MR} decreases the phase of the MA open loop TF at gain crossover frequency, and thus reduces the phase margin of G_T. It is also possible to increase the low frequency attenuation of S_M by incorporating lag-compensation in the MA outer loop compensator design describe in section III-B.2.

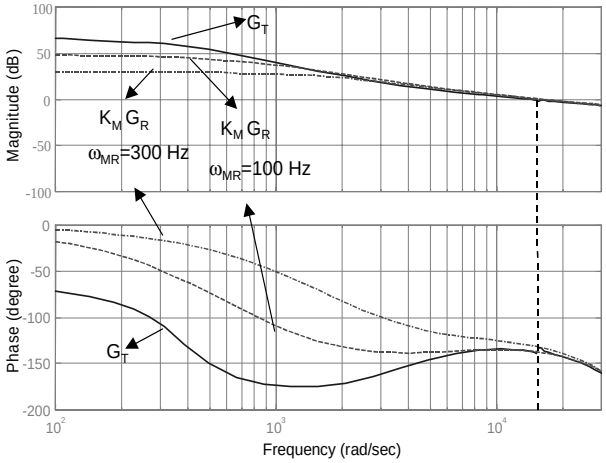

Fig. 8. Bode plots of G_T and $K_M\,G_R$ for ω_{MR}=300 Hz and ω_{MR}=100 Hz

D. SIMO track-following controller design

The design procedure describe in section III can also be applied to SIMO control architectures, where the RPES is not available, by incorporating an open loop observer to estimate the RPES, as shown in Fig. 9, where the open loop observer $\hat{G}_R$, generates the RPES estimate signal $\hat{RPES}$. In the block diagram in Fig. 9 the transfer function $\hat{G}_R$ is the same as that of G_R in Eq. (15). By Eq. (10), the combined action of the open loop observer G_R and the RPES minor loop compensator K_{RS}/K_{RR} is equivalent to the notch filter, K_{MN}, which is defined by

$$K_{MN}(q^{-1}) = \frac{1}{K_{RS}}\left(1 - \hat{G}_R\,K_{RR}\right) = \frac{A_o(q^{-1})}{A_R(q^{-1})}\,, \qquad (19)$$

where $A_o(q^{-1})$ is estimate of the MA open loop pole polynomial, given by Eq. (8), and $A_R(q^{-1})$ is the desired pole polynomial of G_R. The notch filter K_{MN} can be made more robust to variations in the MA's natural resonance

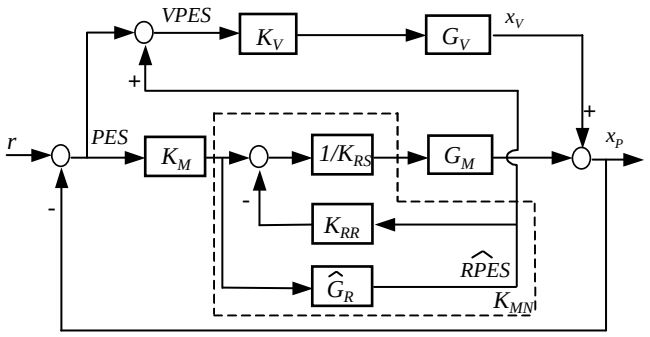

Fig. 9. SIMO control design block diagram

frequency, ω_{MO} in (10), by making the damping ratio ζ_{MO} 10 times larger than its nominal value. This results in a "wider" notch filter.

E. Design and simulation results

In this section we show simulation results of the proposed MIMO and SIMO designs, when the PES sampling frequency is 20 kHz. Fig. 10 shows the gain Bode plot of the closed loop sensitivity TF from track runout r to PES, for both the MIMO and SIMO designs. The design parameters used in the simulations were $\omega_{VC} = 500Hz$ $\omega_{MR} = 300Hz$, $\zeta_{MR} = 1$, $\omega_{MC} = 3000Hz$ and $\zeta_{MC} = 1$. In the case of the MIMO design, K_V is 4^{th} order, both K_M and K_{RS}/K_{RR} are $1st$ order. The gain crossover frequency (GCF), gain margin (GM), and phase margin (PM) of open loop TF from r to x_p are respectively, 2337 Hz, 9.1 dB, and 42.3°. In the case of the SIMO design, the combined VCM loop compensator is 5^{th} order, and the combined MA loop compensator is 4^{th} order. The GCF, GM, and PM of open loop TF from r to x_p are respectively, 2432 Hz, 8.7 dB, and 24.7°. Fig. 11 and Fig. 12 respectively show the 1 μm

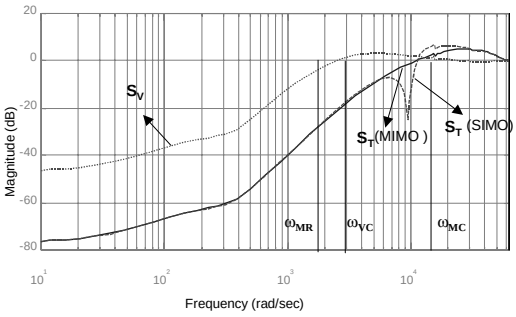

Fig. 10. S_V and S_T Magnitude Bode plot

time domain step responses of the MIMO and SIMO designs. The SIMO controller response has a larger overshoot and exhibits more residual vibrations than the MIMO controller response. This is due to the MA's resonance poles are not being exactly canceled by the notch filter K_{MN} in Eq. (19), in order to guarantee the stability robustness of the designed controller to MA resonance frequency variations.

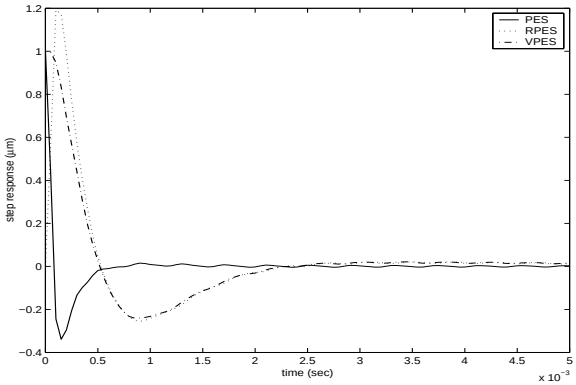

Fig. 11. Step response of MIMO design

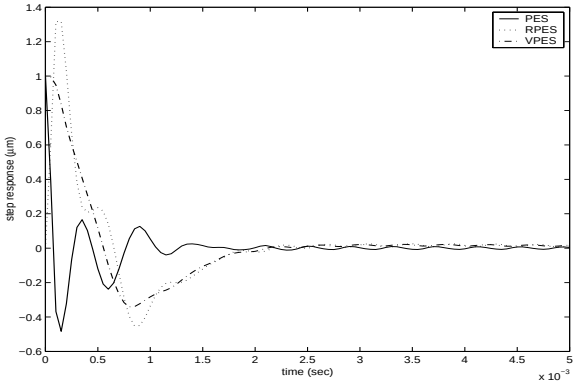

Fig. 12. Step response of SIMO design

IV. Robust stability analysis using μ

The robust stability of the decouple MIMO and SIMO designs presented in section III can be analyzed using the μ analysis methodology [13]. μ, the structured singular value, is a measure of how big must a perturbation to a system be, in order to make the closed loop system unstable. For the case of MEMS based dual-stage servo systems, we are particularly concerned with the robust stability of the close loop system to variations in the resonance frequency (or equivalently the stiffness) of the MA, unmodeled high frequency structural resonance modes of the VCM actuator and variations in the DC gain of VCM. In the μ robust stability analysis framework, model uncertainties are represented using linear fractional transformations (LTF). Fig. 13 shows the block diagram that was used to described structured uncertainties in our system. Three model uncertainties δ_1, δ_2 and δ_3, are considered in Fig. 13: δ_1 represents the additive uncertainty used to describe the VCM unmodeled resonance dynamics and W_{UV} is the frequency shaped weight for δ_1. An uncertainty with the size of the amplitude of the biggest resonance peak of the VCM model was used for δ_1. δ_2 is the parameter uncertainty that represents VCM loop gain variations, a $\pm$ 10% variation is considered. δ_3 is the parameter uncertainty that represents MA stiffness variations, a $\pm$ 10% variation is considered.

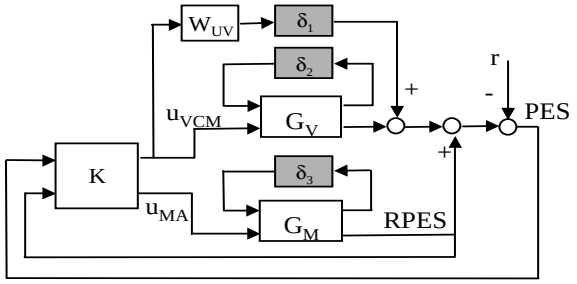

Fig. 13. μ-synthesis design block diagram

Fig. 14 shows the resulting robust stability μ plots. It shows a peak μ value of β_{MIMO}=0.18 for the MIMO design and a peak μ value of β_{SIMO}=0.49 for the SIMO design. Thus, both designs can maintain stability for the structured uncertainties described above and the MIMO design has better stability robustness than the SIMO design, as expected.

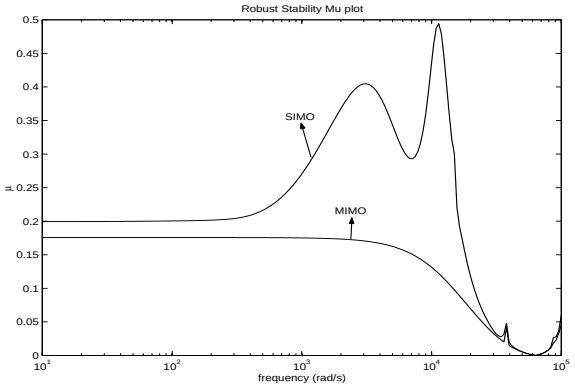

Fig. 14. Stability μ plot

Of these three structured uncertainties, it is the variations in the MA's stiffness, which appear to have the most significant detrimental effect on the performance of both the MIMO and SIMO designs, even when the closed loop system remains stable. For the MIMO design, variations in the stiffness of the MA's flexures produce variations in its DC gain, which have a large effect on the gain of the open loop transfer function G_T, which is dominated at low frequencies by the last term of Eq. (5). For the SIMO design, the lightly damped MA resonance mode can be excited if there is a significant mismatch between the actual MA resonance frequency and its nominal value.

V. RPES minor loop self-tuning control

A direct self-tuning algorithm can be incorporated into the MA $RPES$ minor loop, to compensate for MA resonance frequency variations. It should be emphasized that these variations are due to the fabrication process. Thus, the resonance frequency for a particular MA does not change once it is installed on the HDA. Thus, nominal performance can be achieved in every system after the control parameters are tuned. The parameter adaptation

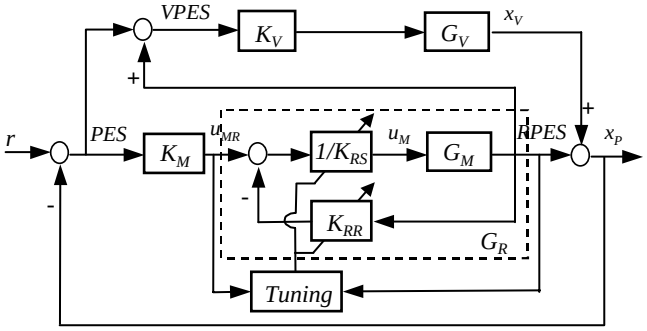

Fig. 15. Self-tuning control of the MA

algorithm (PAA) that will be presented is based on the pole placement design and requires measurement of MA's relative position error signal $RPES$.

Consider the MA open loop transfer function in Eq. 8. Since the MA's resonance mode is lightly damped, the zero z_o in Eqs. (9) and (13) remains fairly invariant with $\pm 15\%$ variations in the resonance frequency ω_{MO} and moreover $z_o \approx 1$. Thus, it is possible to factor out the "known" term $(1 + z_o q^{-1})$ from the Diophantine equation (14). The resulting minor-loop RPES closed loop dynamics is given by

$$\begin{aligned} A_c(q^{-1})RPES(k) &= q^{-1}b_0(1 + z_o q^{-1})[K_{RS}(q^{-1})u_{MR}(k) \\ &\quad + K_{RR}(q^{-1})RPES(k)] \end{aligned} \tag{20}$$

where u_{MR} is the control input to the MA. Defining:

$$\begin{aligned} S(q^{-1}) &= b_0 K_{RS}(q^{-1}) = s_0 + s_1 q^{-1} \\ R(q^{-1}) &= b_0 K_{RR}(q^{-1}) = r_0 + r_1 q^{-1} \end{aligned}$$

the regressor vector, $\phi(k)$ and filtered regressor vector, $\phi_f(k)$,

$$\begin{aligned} &\phi(k) = [u_{MR}(k)\ u_{MR}(k-1)\ RPES(k)\ RPES(k-1)] \\ &A_c(q^{-1})\phi_f(k) = (1 + z_o q^{-1})\phi(k) \end{aligned}$$

and the controller parameter vector $\theta = [s_0\ s_1\ r_0\ r_1]^T$, the closed loop $RPES$ dynamics (20)can be rewritten as

$$RPES(k) = \theta^T \phi_f(k-1)\,. \tag{21}$$

From Eq. (21), the controller parameter vector estimate $\hat{\theta}(k) = [\hat{s}_0(k)\ \hat{s}_1(k)\ \hat{r}_0(k)\ \hat{r}_1(k)]^T$ can be updated using a standard recursive least square algorithm [11]:

$$\begin{aligned} \hat{\theta}(k+1) &= \hat{\theta}(k) + P(k)e^o(k) \\ e^o(k) &= RPES(k) - \hat{\theta}^T(k-1)\phi_f(k-1) \end{aligned}$$

$$P(k) = \frac{1}{\lambda}\left[P(k-1) - \frac{P(k-1)\phi_f(k-1)\phi_f^T(k-1)P(k-1)}{\lambda + \phi_f^T(k-1)P(k-1)\phi_f(k-1)}\right],$$

where λ is the least square forgetting factor, and the control law is

$$\hat{S}(k, q^{-1})u_{MR}(k) = \hat{s}_o(k)u_M(k) - \hat{R}(k, q^{-1})\,RPES(k) \tag{22}$$

with

$$\begin{aligned}\hat{S}(k,q^{-1}) &= \hat{s}_0(k)+\hat{s}_1(k)q^{-1}\\ \hat{R}(k,q^{-1}) &= \hat{r}_0(k)+\hat{r}_1(k)q^{-1},\end{aligned}$$

and $u_M(k)$ being the output of the MA fixed outer loop compensator K_M, $u_M(k)$ being the control input to the MA .

Fig. 16 shows the simulated response of the control parameters estimates using the recursive least square algorithm for the MIMO design, when the real MA resonance frequency is 1.5 times of its nominal value. As shown in the figure, the controller parameters converge to their desired values. The parameters tuning convergence does not need additional fictitious excitation since it is a direct self-tuning scheme. Similar responses were obtain when the real resonance frequency is half the nominal value and for the SIMO architecture.

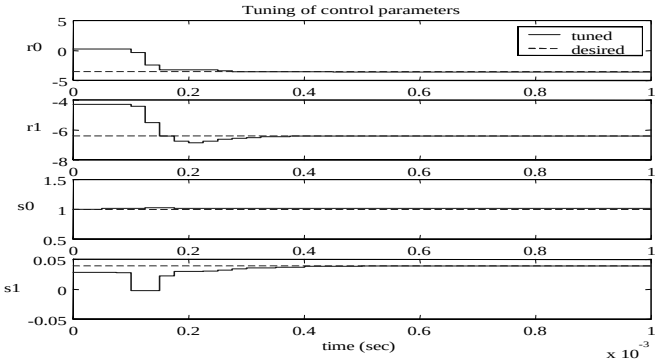

Fig. 16. Control parameters adaptation response

It should be emphasized that the variations in the MA's resonance frequency ω_{MO} are due to the fabrication process, and ω_{MO} does not change after the MA has been fabricated. Thus, the self-tuning algorithm only needs to run during the product test stage and at a slower sampling rate. Thus, the computation needed for the self-tuning algorithm will not be a problem. The proposed self-tuning scheme requires the measurement of the $RPES$. However, the scheme can also be used to tune the SIMO track-following servo by replacing the signal $RPES(k)$ in Eq. (22) by $\hat{RPES}(k)$, the output of the open loop observor $\hat{G}_R$. Thus, for the SIMO case, the self-tuning algorithm can also be implemented during the factory test stage, utilizing additional electronics to measure the $RPES$. Once convergence of the parameters is achieved and the controller is tuned, the SIMO controller can operate without measurement of the $RPES$.

VI. Conclusions

MIMO and SIMO track-following controllers for MEMS based dual-stage servo systems were designed using a decoupled discrete time pole placement design methodology. Both designs are robust to variations in the MA's resonance frequency. The MIMO design can achieve a superior robustness and performance, partly due to the additional RPES sensor. The decoupled MIMO design presented in this paper requires considerable fewer computations than the μ synthesis design in [9]. Self-tuning control can be used to tune the control parameters, during the product test stage, to compensate for variations in the microactuator's resonance frequency, and restore nominal controller performance.

Acknowledgments

The authors thank L.-S. Fan and W.-M. Lu from IBM, M. Kobayashi from Hitachi and the industrial participants of the NSIC EHDR servo team for their comments and useful discussions.

References

[1] L.-S. Fan, T. Hirano, J. Hong, P. R. Webb, W.H. Juan, W. Y. Lee, S. Chan, T. Semba, W. Imaino, T.S. Pan, S. Pattanaik, F.C. Lee, I. McFadyen, S. Arya, and R. Wood, "Electrostatic microactuator and design considerations for hdd application," *IEEE Transactions on Magnetics*, vol. 35, no. 2, pp. 1000–1005, March 1999.

[2] D. Horsley, N. Wongkomet, R. Horowitz, and A. Pisano, "Precision positioning using a microfabricated electrostatic actuator," *IEEE Transactions on Magnetics*, vol. 35, no. 2, pp. 993–999, March 1999.

[3] T. Hirano, L.-S. Fan, W. Y. Lee, J. Hong, W. Imaino, S. Pattanaik, S. Chan, R. Horowitz, S. Aggarwal, D.A. Horsley "High-Bandwidth High-Accuracy Rotary Microactuators for Magnetic Disk Drive Tracking Servos," *IEEE/ASME Transactions on Mechatronics*, vol. 3, no. 3, pp. 156–165, September 1998.

[4] W. Guo, S. Weerasooriya, T. B. Goh, Q. H. Li, C. Bi, K. T. Chang and T. S. Low, "Dual stage actuators for high density rotating memory devices," *IEEE Transactions on Magnetics*, vol. 34, no. 2, pp. 450–455, November 1998.

[5] S. Koganezawa, Y. Uematsu, and T. Yamada, "Dual-Stage Actuator System for Magnetic Disk Drives Using a Shear Mode Piezoelectric Microactuator," in *IEEE Transactions on Magnetics*, vol. 35, no. 2, pp. 988–992, March 1999.

[6] S. J. Schroeck and W. C. Messner, "Dual-stage track-following servo design for hard disk drive," in *Proceedings of the American Control Conference*, June 1999, pp. 4122–4126.

[7] X. Hu, Wei Guo, T. Huang, and B. M. Chen, "Discrete time LQG/LTR dual-stage controller design and implementation for high track density HDDs," in *Proceedings of the American Control Conference*, pp. 4111–4115. June 1999,

[8] T. Semba, T. Hirano, L.-S. Fan, "Dual-Stage Servo Controller for HDD Using MEMS Actuator," in *IEEE Transactions on Magnetics*, vol. 35, no. 5, pp. 2271–2273, Semptember 1999.

[9] D. Hernandez, S.-S. Park, R. Horowitz, and A. K. Packard, "Dual-stage track-following servo design for hard disk drive," in *Proceedings of the American Control Conference*, June 1999, pp. 4188–4121.

[10] K. Mori, T. Munemoto, H. Otsuki, Y. Yamaguchi, and K. Akagi, "A dual-stage magnetic disk drive actuator using a piezoelectric device for a high track density," *IEEE Transactions on Magnetics*, vol. 27, no. 6, pp. 5298–5300, November 1991.

[11] K. J. Åström and B. Wittenmark, *Computer Controlled Systems: Theory and Design*, Prentice-Hall, 1984.

[12] M. T. Whilte and W.-M. Lu, "Hard disk drive bandwidth limitations due to sampling frequency and computational delay." *Proceedings of the 1999 IEEE/ASME International Conference on Intelligent Mechatronics*, pp. 120–125, Sep. 1999.

[13] G. J. Balas, J. C. Doyle, K. Glover, A. Packard, R. Smith, "m-Analysis and Synthesis ToolBox," MUSYN Inc. and The MathWorks, Inc., 1995